Soil Dynamics and Earthquake Engineering 124 (2019) 72–85

Contents lists available at ScienceDirect

Soil Dynamics and Earthquake Engineering

journal homepage: www.elsevier.com/locate/soildyn

Investigating ground vibration induced by moving train loads on unsaturated ground using 2.5D FEM

Guangyun Gao[a,b,*], Shaofeng Yao[a,b], Jun Yang[c], Juan Chen[a,b]

[a] College of Civil Engineering, Tongji University, Shanghai, 200092, China
[b] Key Laboratory of Geotechnical and Underground Engineering of Ministry of Education, Tongji University, Shanghai, 200092, China
[c] Department of Civil Engineering, The University of Hong Kong, Hong Kong, China

ARTICLE INFO

Keywords:
2.5D FEM
High speed train
Moving load
Unsaturated soil
Ground vibration
Excess pore pressure

ABSTRACT

A two-and-a-half-dimensional finite element method (2.5D FEM) is applied to investigate the dynamic response of an unsaturated ground subjected to moving loads caused by high-speed train. The partial differential equations of unsaturated porous medium in frequency domain are deduced based on the equations of motion and mass conservation of three phases, with consideration of the compressibility of solid grain and pore fluid. Governing equations of unsaturated soil in 2.5D FE form are derived by using the Fourier Transform with respect to the load moving direction. The track structure is simplified as an Euler beam resting on the unsaturated porous half-space and the viscous-elastic artificial boundaries are used to avoid the energy reflection from the boundary. Numerical simulations demonstrate effects of the degree of water saturation and train speed to the ground vibration and the excess pore water pressure. It is concluded that the degree of water saturation has a different influence on the ground displacement and acceleration. The gas phase has varied influence to the ground displacement amplitude at different train speed level at the track center. A very small amount of gas in the saturated ground largely increases the ground acceleration amplitude at a given train speed. Ground displacements attenuate rapidly with almost the same rate for both high and low train speeds near the track center. The maximum amplitude of excess pore water pressure is located at 1.5–2.0 m beneath the ground surface and decreases significantly as the degree of water saturation decreases.

1. Introduction

In recent years, the high-speed-railway has been developed as a quick and convenient means of mass transportation in China. Evaluating the train-caused ground vibration and its impact on the adjacent environment is hence an important design consideration.

Investigations concerning the ground vibration induced by moving loads dated back to 1950s, which have been partly reviewed by Beskou and Theodorakopoulos [1]. Many investigations were conducted by analytical means assuming a homogeneous elastic half-space [2,3] or by using semi-analytical models for a multi-layered ground [4]. The FEM, the BEM or the FEM/BEM hybrid schemes [5–8] were also widely used considering their advantages at dealing with the irregularities of the geometry and material. By assuming the material and geometric properties to be constant along the load-moving direction, only the profile normal to the load-moving direction needs be considered, which is two-dimensional in nature. However, if the effect of the moving loads is to be considered, then the problem is somewhat between two- and three-dimensional (2.5D) [9,10]. Such an idea was firstly proposed by Hwang and Lysmer [11] in studying the response of an underground structure to traveling seismic waves, and was also used by Barros and Luco [12] to obtain the steady-state displacements and stresses within a multi-layered viscoelastic half-space generated by a buried or surface point load moving with constant speed. Yang and Hung [9,10] used the 2.5D FEM to study the 3D ground dynamic response under train loads, considering the discrete sleeper supports of the train tracks. The same concept was also adopted by Takemiya [13] and Bian et al. [14,15] in the study of the environmental vibration caused by the train loads. These studies simplified the subgrade soil as single-phase elastic or visco-elastic soil.

Biot [16,17] proposed the elasto-dynamic theory for saturated porous media, making it possible to study the dynamic response of saturated ground under moving loads [18,19]. Siddharthan et al. [20] and Theodorakopoulos et al. [21,22] have studied the response of a poro-elastic half-space subjected to moving loads analytically and numerically. Lu and Jeng [23] presented an analytical solution for the

* Corresponding author. Department of Geotechnical Engineering, Tongji University, Shanghai, 200092, China.
E-mail addresses: gaogy@tongji.edu.cn, gaoguangyun@263.net (G. Gao).

https://doi.org/10.1016/j.soildyn.2019.05.034
Received 25 January 2019; Received in revised form 16 April 2019; Accepted 21 May 2019
Available online 30 May 2019

dynamic response of a half-space porous medium subjected to a moving point load using the Holmholtz decomposition and Fourier Transformation method. Using Fourier Transform, Lefeuve-Mesgouez and Mesgouez [24] presented a 3D semi-analytical approach to study the displacements of a poro-visco-elastic multi-layered half-space induced by harmonic surface loads moving at a constant speed. Considering the track system, Cai et al. [25,26] investigated the dynamic responses of a saturated half-space under different train moving load patterns. Yang et al. [27] semi-analytically studied the vibration of a water-saturated poro-elastic ground induced by high speed train, considering the discrete sleeper effect, damping property and the intrinsic permeability of the soil. Gao et al. [28–30] investigated the dynamic responses of saturated soils (including homogeneous, transversely isotropic and layered) under moving loads using the 2.5D FEM.

The ground model is of greatly important for the accuracy of the numerical simulation of the track-ground response under moving loads. Most previous studies treated ground as a single-phase or water-saturated poro-elastic medium. In arid and semi-arid areas, however, the subsoil is often in an unsaturated state due to large amounts of evaporation and transpiration [31]. Jafarzadeh and Sadeghi [32], Vardoulakis and Beskos [33] and Yang and Sato [34] all pointed out that the degree of saturation has a significant influence on dynamic characteristics of the ground. In contrast to the scenario of saturated soil, even a small decrease of the degree of water saturation can greatly influence the displacement of the soil skeleton and the excess pore water pressure [32,33,35,36]. Treating the soil as a single-phase or saturated medium is not adequate in seeking more accurate estimation of ground vibration caused by high-speed trains.

Considering the irregularities of the geometry and material of the ground and track systems, the FEM is perhaps the best method with respect to efficiency, versatility and availability without compromising accuracy [1]. Particularly, the 2.5D FEM mentioned above is especially useful when the applied load and structural response are 3D while the structure itself is 2D [9,11,12,29]. The finite element discretization is required only in a section perpendicular to the track direction in 2.5D FEM formulation, which is simpler than the full 3D FEM formulation. Solving the 3D problem using a 2D plane model can significantly reduce the computation cost without losing accuracy at the same time, and the results can be quickly derived in a single computation. While the 2.5D FEM formulations have been developed for dynamic problems involving single-phase elastic [9,10,12–15] or two-phase saturated media [28–30], to the authors' best knowledge, they are not yet available for the unsaturated ground model.

In this study, a 2.5D FEM formulation for studying the vibration of an unsaturated ground caused by moving high-speed train loads is presented. The partial differential equations of unsaturated porous medium in frequency domain are deduced based on the equations of motion and mass conservation of three phase, with consideration of the compressibility of solid grain and pore fluid. By using the Galerkin method and applying the Fourier Transform with respect to the load-moving direction, the 2.5D FEM formulation of the governing equations of unsaturated medium in frequency-wave number domain are then derived. The track structure (including the track and the embankment) is simplified as an Euler beam resting on the unsaturated ground, which is discretized by 2.5D quadrilateral elements. The viscous-elastic artificial boundaries are used to avoid the energy reflection from the boundary. The solution in the frequency-wave number domain is transformed to the time-space domain through the Fast Fourier Transform (FFT). Numerical calculations are presented to show effects of the degrees of water saturation and train speeds on the ground vibration induced by the moving train loads.

2. 2.5D FEM formulations for unsaturated ground-track model

2.1. Governing equation of unsaturated poro-elastic medium in frequency domain

The following assumptions are made to the continuous three-phase porous medium: (1) the mechanical and permeability properties are uniform; (2) the movement of the water and gas obey the generalized Darcy's law; (3) the soil particle density is related to the fluid pressure and volume deformation, and the water and gas densities are functions of their own pore pressures, respectively. The double Fourier Transform with respect to t and x is defined as $\bar{u}(\xi_x, y, z, \omega) = \int_{-\infty}^{+\infty}\int_{-\infty}^{+\infty} u(x, y, z, t)e^{i\xi_x x}e^{-i\omega t}dxdt$, where ω and ξ_x are the frequency variable and the wave number variable corresponding to time t and space variable x.

The mass conservation of solid particle can be expressed as [31]:

$$(1-n)\frac{\dot{\rho}_s}{\rho_s} - \dot{n} + (1-n)\dot{u}_{i,i} = 0 \tag{1}$$

where ρ_s is the soil particle density; n is the soil porosity; u is the displacement of soil particle; "·" represents the first derivative with time.

The influence of water pressure and volume deformation to the density of soil particle can be expressed as [31]:

$$(1-n)\frac{\dot{\rho}_s}{\rho_s} = \frac{\alpha-n}{K_g}\dot{p}_c - (1-\alpha)\dot{u}_{i,i} \tag{2}$$

where $\alpha = 1\text{-}K_{sk}/K_g$ is Biot coefficient, K_{sk} is the bulk modulus of soil skeleton, K_g is the bulk modulus of soil particle; $u_{i,i}$ is volume deformation of soil; p_c is the equivalent pore pressure of unsaturated soil and it is assumed that $p_c = S_r p^w + (1\text{-}S_r)p^a$, where S_r is the degree of water saturation, p^w and p^a are the pore water pressure and pore gas pressure, respectively [31]. Substituting Eq. (2) into Eq. (1) yields:

$$\dot{n} = \frac{\alpha-n}{K_g}\dot{p}_c + (\alpha-n)\dot{u}_{i,i} \tag{3}$$

The mass conservation of pore water can be expressed as [31]:

$$\frac{\partial}{\partial t}(\rho_w n S_r) + \rho_w n S_r u^w_{i,i} = 0 \tag{4}$$

where ρ_w is the water density; u^w is the water displacement. The relationship between water density and water pressure can be expressed as [31]:

$$\frac{\mathrm{d}\rho_w}{\rho_w} = \frac{\mathrm{d}p^w}{K_w} \tag{5}$$

where K_w is the bulk modulus of pore water. By substituting Eqs. (3) and (5) into Eq. (4), one can get:

$$S_r\left[\frac{\alpha-n}{K_g}\dot{p}_c + (\alpha-n)\dot{u}_{i,i}\right] + \frac{nS_r}{K_w}\dot{p}^w + n\dot{S}_r + nS_r\dot{u}^w{}_{i,i} = 0 \tag{6}$$

The soil-water characteristic curve (SWCC) [31] is used to describe the relationship between the degree of water saturation and matric suction:

$$S_r = S_r(s) = S_r(p^a - p^w) \tag{7}$$

where $s = p^a\text{-}p^w$ is matric suction.

Under the assumption of small deformation, the continuous equation of pore water can be obtained by substituting Eq. (7) into Eq. (6):

$$A_{11}\dot{p}^w + A_{12}\dot{p}^a + A_{13}\dot{u}_{i,i} + A_{14}\dot{u}^w{}_{i,i} = 0 \tag{8}$$

where the four coefficients A_{11}, A_{12}, A_{13}, A_{14} are listed in Appendix A.

The mass conservation of pore gas can be expressed as [31]:

$$\frac{\partial(n(1-S_r)\rho_a)}{\partial t} + n(1-S_r)\rho_a\dot{u}^a_{i,i} = 0 \tag{9}$$

where ρ_a is the gas density; u^a the displacement of the pore gas. The

relation between gas compression deformation and gas pressure can be expressed as [31]:

$$\frac{\mathrm{d}\rho_a}{\rho_a} = \frac{\mathrm{d}p^a}{K_a} \tag{10}$$

where K_a is the bulk modulus of pore gas.

Substituted Eqs. (3) and (10) into Eq. (9) results:

$$(1-S_r)\left[\frac{\alpha-n}{K_g}\dot{p}_c + (\alpha-n)\dot{u}_{i,i}\right] + n(1-S_r)\frac{\dot{p}^a}{K_a} - n\dot{S}_r + n(1-S_r)\dot{u}^a{}_{i,i} = 0 \tag{11}$$

Under the small deformation assumption, the continuous equation of pore gas can be obtained by substituting Eq. (7) into Eq. (11):

$$A_{21}\dot{p}^w + A_{22}\dot{p}^a + A_{23}\dot{u}_{i,i} + A_{24}\dot{u}^a{}_{i,i} = 0 \tag{12}$$

where the four coefficients A_{21}, A_{22}, A_{23}, A_{24} are listed in Appendix A.

According to the generalized Darcy's law, the seepage equations of pore water and pore gas are [31]:

$$nS_r(\dot{u}_i^w - \dot{u}_i) = -\frac{k_w}{\rho_w g}(p^w_{,i} + \rho_w \ddot{u}_i^w) \tag{13}$$

$$n(1-S_r)(\dot{u}_i^a - \dot{u}_i) = -\frac{k_a}{\rho_a g}(p^a_{,i} + \rho_a \ddot{u}_i^a) \tag{14}$$

where "·" denotes the second order derivative with time; k_w and k_a are the permeability coefficients of pore water and pore gas. By applying the Fourier Transform to Eqs. (13) and (14) with respect to time t, the average displacements of pore water and gas in frequency domain can be obtained:

$$\tilde{u}_i^w = \frac{F_w\tilde{u}_i - \tilde{p}^w_{,i}}{F_w - \rho_w\omega^2} \tag{15}$$

$$\tilde{u}_i^a = \frac{F_a\tilde{u}_i - \tilde{p}^a_{,i}}{F_a - \rho_a\omega^2} \tag{16}$$

where "~" represents the solution in frequency domain; $F_a = n(1\text{-}S_r)\rho_a g\omega i/k_a$, and $F_w = nS_r\rho_w g\omega i/k_w$. Applying the Fourier Transform with respect to t in Eqs. (8) and (12), and with Eqs. (15) and (16), the continuous equations of pore water and pore gas in frequency domain are obtained as follows:

$$A_{11}\tilde{p}^w + A_{12}\tilde{p}^a + \left(A_{13} + \frac{A_{14}F_w}{F_w - \rho_w\omega^2}\right)\tilde{u}_{i,i} - \frac{A_{14}}{F_w - \rho_w\omega^2}\tilde{p}^w_{,ii} = 0 \tag{17}$$

$$A_{21}\tilde{p}^w + A_{22}\tilde{p}^a + \left(A_{23} + \frac{A_{24}F_a}{F_a - \rho_a\omega^2}\right)\tilde{u}_{i,i} - \frac{A_{24}}{F_a - \rho_a\omega^2}\tilde{p}^a_{,ii} = 0 \tag{18}$$

In frequency domain, the dynamic equilibrium differential equation of unsaturated soil neglecting the body force can be expressed as Eq. (19). Under the assumption of small deformation and the Bishop effective stress principle, the stress-strain relation of unsaturated soil and the geometry equation of soil skeleton can be respectively expressed as Eqs. (20) and (21) [31]:

$$\tilde{\sigma}_{ij,j} = (1-n)\rho_s\omega^2\tilde{u}_i + nS_r\rho_w\omega^2\tilde{u}_i^w + n(1-S_r)\rho_a\omega^2\tilde{u}_i^a \tag{19}$$

$$\tilde{\sigma}_{ij} = 2\mu\tilde{\varepsilon}_{ij} + \lambda\delta_{ij}\tilde{\varepsilon}_{kk} - \delta_{ij}\alpha\tilde{p}_c \tag{20}$$

$$\tilde{\varepsilon}_{ij} = \frac{1}{2}(\tilde{u}_{i,j} + \tilde{u}_{j,i}) \tag{21}$$

With Eqs. (15), (16), (19)–(21) the dynamic equilibrium differential equation of unsaturated soil in frequency domain can be expressed by soil particle displacement, pore water and pore gas pressure as follow:

$$\tilde{\sigma}_{ij,j} + \omega^2\left[(1-n)\rho_s + \frac{nS_r\rho_w F_w}{F_w - \rho_w\omega^2} + \frac{n(1-S_r)\rho_a F_a}{F_a - \rho_a\omega^2}\right]\tilde{u}_i - \frac{\omega^2 nS_r\rho_w}{F_w - \rho_w\omega^2}\tilde{p}^w_{,i} - \frac{\omega^2 n(1-S_r)\rho_a}{F_a - \rho_a\omega^2}\tilde{p}^a_{,i} = 0 \tag{22}$$

where $\tilde{\sigma}_{ij,j}$, $\tilde{\varepsilon}_{ij}$ are the total stress and strain tensor of the unsaturated soil in frequency domain; δ_{ij} is Kronecker symbol; λ and μ are the Lame constants of the soil. The complex form of Lame constants, λ^c and μ^c are used to replace the λ and μ in Eq (20) to reflect damping effects of the soil:

$$\lambda^c = (1+2i\eta_s)\lambda,\ \mu^c = (1+2i\eta_s)\mu \tag{23}$$

where η_s is the damping coefficient of the unsaturated soil.

Eqs. (17), (18) and (22) is the governing partial differential equations of unsaturated soil in frequency domain, which will be solved in the following section.

2.2. 2.5D FE solution of unsaturated poro-elastic medium

For drainage boundary, the boundary conditions of Eqs. (17), (18) and (22) can be summarized as follows:

(1) Boundary conditions at stress boundary S_σ:

$$\tilde{\sigma}_{ij}n_j = \tilde{T}_i \tag{24}$$

(2) Boundary conditions at flux boundary S_p:

$$p'^f{}_{,j}n_j = -\frac{\rho_f g}{k_f}\tilde{\mathbf{v}}_f,\ (f = w,\ a) \tag{25}$$

where $\tilde{T}_i$, p'^f are the stress and pore pressure at the boundary in frequency domain; n_j is the exterior normal direction vector; $\mathbf{v}_f$ is the velocity of the fluid at the boundary; ρ_f and k_f are the fluid density and permeability coefficient, where $f = w$, a represent pore water and pore gas, respectively; g is the gravity acceleration.

Using Galerkin method to Eqs. (22) and (24) and to Eqs. (17), (18) and (25), and by introducing the variation of virtual displacement $\delta\tilde{u}_i^*$ and virtual pressure $\delta\tilde{p}^f$ in frequency domain as the weighted function, we can obtain the equivalent integral form of the governing equation of unsaturated soil as follows:

$$\int \delta\tilde{u}_i^*\left[\tilde{\sigma}_{ij,j} + \omega^2\left[(1-n)\rho_s + \frac{nS_r\rho_w F_w}{F_w-\rho_w\omega^2} + \frac{n(1-S_r)\rho_a F_a}{F_a-\rho_a\omega^2}\right]\tilde{u}_i - \frac{\omega^2 nS_r\rho_w}{F_w-\rho_w\omega^2}\tilde{p}^w_{,i} - \frac{\omega^2 n(1-S_r)\rho_a}{F_a-\rho_a\omega^2}\tilde{p}^a_{,i}\right]dV - \int \delta\tilde{u}_i^*(\tilde{\sigma}_{ij}n_j - \tilde{T}_i)dS = 0 \tag{26a}$$

$$\int_v \delta\tilde{p}^w\left[-\frac{A_{14}}{F_w-\rho_w\omega^2}\tilde{p}^w_{,ii} + \left(A_{13} + \frac{A_{14}F_w}{F_w-\rho_w\omega^2}\right)\tilde{u}_{i,i} + A_{11}\tilde{p}^w + A_{12}\tilde{p}^a\right]dv + \int_{S_p}\delta\tilde{p}^w\frac{A_{14}}{F_w-\rho_w\omega^2}\left(\frac{\partial p'^w}{\partial\vec{n}} + \frac{\rho_w g}{k_w}\tilde{v}_w\right)ds = 0 \tag{26b}$$

$$\int_v \delta\tilde{p}^a\left[-\frac{A_{24}}{F_a-\rho_a\omega^2}\tilde{p}^a_{,ii} + \left(A_{23} + \frac{A_{24}F_a}{F_a-\rho_a\omega^2}\right)\tilde{u}_{i,i} + A_{21}\tilde{p}^w + A_{22}\tilde{p}^a\right]dv + \int_{S_p}\delta\tilde{p}^a\frac{A_{24}}{F_a-\rho_a\omega^2}\left(\frac{\partial p'^a}{\partial\vec{n}} + \frac{\rho_a g}{k_a}\tilde{v}_a\right)ds = 0 \tag{26c}$$

By using parts integration property and Gauss formula, the equivalent integral weak form of Eq. (26) can be obtained as follows:

$$\int_v \delta\tilde{\varepsilon}_i^*\tilde{\sigma}'_{ij}dv - \int_v \delta\tilde{u}_i^*\tilde{f}_i dv - \int_v \delta\tilde{u}_i^* A_{31}\tilde{u}_i dv + \int_v \delta\tilde{u}_i^* A_{32}\tilde{p}^w_{,i}dv + \int_v \delta\tilde{u}_i^* A_{33}\tilde{p}^a_{,i}dv - \int_v \delta\tilde{\varepsilon}_i^*\delta_{ij}\alpha S_r\tilde{p}^w dv - \int_v \delta\tilde{\varepsilon}_i^*\delta_{ij}\alpha(1-S_r)\tilde{p}^a dv = \int_{S_\sigma}\delta\tilde{u}_i^*\tilde{T}_i ds \tag{27a}$$

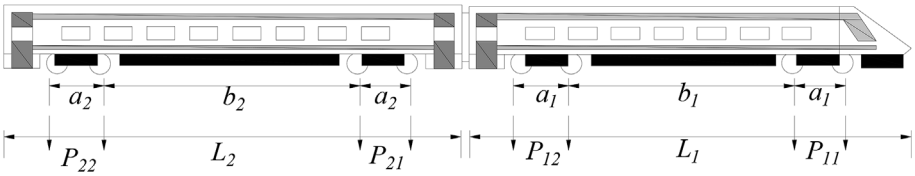

Fig. 1. Geometric profile of train wheel loads.

$$\frac{A_{14}}{F_w-\rho_w\omega^2}\int_v \delta\tilde{p}^w{}_{,i}\tilde{p}^w{}_{,i}dv + A_{11}\int_v \delta\tilde{p}^w\tilde{p}^w dv + \left(A_{13}+\frac{A_{14}F_w}{F_w-\rho_w\omega^2}\right)\int_v \delta\tilde{p}^w\tilde{u}_{i,i}dv + A_{12}\int_v \delta\tilde{p}^w\tilde{p}^a dv = -\frac{A_{14}}{F_w-\rho_w\omega^2}\int_{S_p}\delta\tilde{p}^w\frac{\rho_w g\tilde{v}_w}{k_w}ds \tag{27b}$$

$$\frac{A_{24}}{F_a-\rho_a\omega^2}\int_v \delta\tilde{p}^a{}_{,i}\tilde{p}^a{}_{,i}dv + A_{21}\int_v \delta\tilde{p}^a\tilde{p}^w dv + \left(A_{23}+\frac{A_{24}F_a}{F_a-\rho_a\omega^2}\right)\int_v \delta\tilde{p}^a\tilde{u}_{i,i}dv + A_{22}\int_v \delta\tilde{p}^a\tilde{p}^a dv = -\frac{A_{24}}{F_a-\rho_a\omega^2}\int_{S_p}\delta\tilde{p}^a\frac{\rho_a g\tilde{v}_a}{k_a}ds \tag{27c}$$

By applying the Fourier Transform with respect to x (train moving direction), Eq. (27) in frequency-space domain can be transformed into frequency-wavenumber domain. Meanwhile the 4-node isoparametric element is used for discretization and the interpolation modes in frequency-wave number domain are adopted as follows:

$$\tilde{u} = \mathbf{N}\tilde{u}^e \tag{28a}$$

$$\tilde{p}^f = \bar{\mathbf{N}}\tilde{p}^{fe} \tag{28b}$$

$$\tilde{T} = \mathbf{N}\tilde{T}^e \tag{28c}$$

where "~" represents the variables in frequency-wave number domain, $\tilde{u}^e$ and $\tilde{p}^{fe}$ are nodal displacement and nodal pore pressure; $\mathbf{N} = [\mathrm{I}_3N_1, \mathrm{I}_3N_2, \mathrm{I}_3N_3, \mathrm{I}_3N_4]and\bar{\mathbf{N}} = [N_1, N_2, N_3, N_4]$ are shape function matrices of soil skeleton and pore pressure, where I_3 is the identity matrix and the shape function in $\mathbf{N}$ and $\bar{\mathbf{N}}$ is taken as follow:

$$N_i(\eta, \xi) = \frac{1}{4}(1+\eta_i\eta)(1+\xi_i\xi) \tag{29}$$

where η, ξ are local coordinates of element and η_i, ξ_i are node coefficients of element.

Using the conventional FEM, the corresponding matrix form of Eq. (27) in frequency-wavenumber domain (the so-called 2.5D FEM) can be obtained as follows:

$$(\mathbf{K'_{up}} - \mathbf{M_{up}})\tilde{\mathbf{u}} + (\mathbf{Q'_{up}} - \mathbf{Q_{up}})\tilde{\mathbf{p}}^{\mathbf{w}} + (\mathbf{G'_{up}} - \mathbf{G_{up}})\tilde{\mathbf{p}}^{\mathbf{a}} = \tilde{\mathbf{f}}^{\mathbf{s}}_{\mathbf{up}} \tag{30a}$$

$$\mathbf{H_{md}}\tilde{\mathbf{u}} + (\mathbf{Q_{md}} + \mathbf{Q'_{md}})\tilde{\mathbf{p}}^{\mathbf{w}} + \mathbf{G'_{md}}\tilde{\mathbf{p}}^{\mathbf{a}} = \tilde{\mathbf{f}}^{\mathbf{w}}_{\mathbf{up}} \tag{30b}$$

$$\mathbf{H_{dw}}\tilde{\mathbf{u}} + \mathbf{Q'_{dw}}\tilde{\mathbf{p}}^{\mathbf{w}} + (\mathbf{G_{dw}} + \mathbf{G'_{dw}})\tilde{\mathbf{p}}^{\mathbf{a}} = \tilde{\mathbf{f}}^{\mathbf{a}}_{\mathbf{up}} \tag{30c}$$

where $\mathbf{K'_{up}}$ and $\mathbf{M_{up}}$ are stiffness matrix and mass matrix; $\mathbf{Q'}$ and $\mathbf{Q}$ are liquid contribution matrices; $\mathbf{G'}$ and $\mathbf{G}$ are gas contribution matrices; $\tilde{\mathbf{f}}^{\mathbf{s}}_{\mathbf{up}}$ and $\tilde{\mathbf{f}}^{\mathbf{f}}_{\mathbf{up}}(f = w, a)$ are equivalent nodal force matrix and flux matrix in frequency-wave number domain; others are provided in Appendix B. From Eq. (30), the final 2.5D dynamic equations of unsaturated soil in matrix form can be expressed as follow:

$$\mathbf{KU} = \mathbf{R} \tag{31}$$

where $\mathbf{K}$ is the total assembled stiffness matrix, $\mathbf{U} = [\tilde{\mathbf{u}}\ \ \tilde{\mathbf{p}}^{\mathbf{w}}\ \ \tilde{\mathbf{p}}^{\mathbf{a}}]^T$is the total assembled unknown variable matrix, and $\mathbf{R}$ is the total assembled equivalent nodal force matrix. The detailed elements of $\mathbf{K}$ and $\mathbf{R}$ are provided in Appendix B.

2.3. Track model and train loads in frequency-wave number domain

In this paper, the track structure was simplified as an Euler beam with a width of 3.0 m resting on the unsaturated ground surface subjected to train's moving wheel axle loads. The dynamic equation of the track system in frequency-wave number domain can be expressed as [14]:

$$(EI\xi_x^4 - m\omega^4)\tilde{u}_r = \tilde{f}_{IT}(\xi_x, \omega) + \tilde{p}_0(\xi_x, \omega) \tag{32}$$

where $\tilde{u}_r$ is the track displacement; EI is the bending stiffness of the track system; m is the comprehensive quality of the track and sleepers; $\tilde{f}_{IT}(\xi_x, \omega)$ is the contact reaction force of the ground and $\tilde{p}_0(\xi_x, \omega)$ is the dynamic train load acting on the track.

The moving train is assumed to contain a sequence of N cars, each with four pairs of wheels. The train load acting on the track moving along the x direction with a velocity of V_c can be expressed in the frequency-wave number domain as follows [14]:

$$\tilde{p}_0(\xi_x, \omega) = \frac{2\pi}{V_c}\delta\left(\xi_x - \frac{\omega}{V_c}\right)\chi(\xi_x) \tag{33}$$

where$\chi(\xi_x) = \sum_{n=1}^{N-1}[P_{n1}(1 + exp(-ia_n\xi_x) + P_{n2}(exp(-i(a_n + b_n)\xi_x),\ P_{n1} + exp(-i(2a_n + b_n)\xi_x)]exp(-i\sum_{k=0}^{N-1}L_k\xi_x)$
and P_{n2} are the axle loads for the front and rear bogies; L_0 is the distance to a reference position ahead of the first axle load position and L_i is the ith car length; $a_n a_n$, b_n are the distances between axles. The geometric profile of train wheel loads is shown in Fig. 1.

3. Validation of the proposed model and computational parameters

Eqs. (31) and (32) are the governing equations of the coupled track-ground system, and the sketch map of the 2.5D finite element model of track-ground system is shown in Fig. 2. Rigid connection was used between Euler beam and the ground model and the deformation of the contact point between track and ground is consistent to guarantee the displacement compatibility.

When modeling the space truncated from the infinite domain in numerical simulations, it is necessary to deal with the boundary of the finite domain in order to avoid the energy reflection of outgoing waves from the boundary. A large amount of methods has been used to model the effect of the outgoing wave radiation towards infinity, such as dynamic Infinite Element [37–39], Boundary Element [40] and transmitting boundaries as reviewed by Tsynkov [41]. The visco-elastic

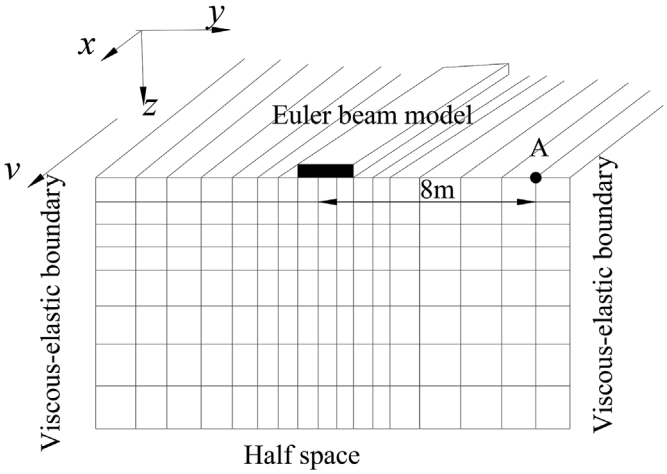

Fig. 2. 2.5D FEM of the track-ground model and the viso-elastic boundary.

boundary can simulate not only the radiation damping of the infinite media but also the elasticity recovery capacity of the far field media outside the boundary with a good stability both under high frequency and low frequency loads [42–44]. Previously, the author [28] have proposed the well worked viscous-elastic dynamic wave absorbing boundary for poro-elastic medium in 2.5D form by assuming that waves are propagating in semi-cylindrical form and achieved the expected goal in application. In this paper, we would still hope to apply this visco-elastic boundary at both sides of the present model considering its suitable and convenient advantages.

The ground layers and properties of soil are the same with site Ledsgard in Sweden operates X2000 train, detailed in literature [13]. Since the ground is symmetric about the track center line, only half of the ground is discretized to reduce the computational time. The width and depth of the calculation model are 60 m and 23.5 m, respectively. Each node of the isoparametric element used in the present 2.5D procedure has three degree of freedom. The mesh sizes of the ground layer are 0.5 m × 0.5 m, and there are totally 5640 elements and 5808 nodes. The time calculation interval is 0.0025 s and the discrete point of wave number is 2048. The solution in time domain will be obtained through FFT method. Measured parameters of strata and train axle loads are listed in Table 1 and Table 2 [13], and the track parameters are listed in Table 3 [14]. When the degree of water saturation $S_r = 0$ in the presented model, the calculation model degenerates into the elastic one, and it can be seen from Fig. 3 that the calculation data are in good agreement with the measured ones [13]. When the degree of water saturation $S_r = 100\%$, the calculation model degenerates into the saturated one. The semi-analytical solution from the previous literature [23] for a 3D homogeneous water-saturated half space subjected to a moving point load with a speed of v in the x-direction was used in the validation of the proposed approach. Three cases with different values of $V_c = 0.1V_s$, $0.5V_s$ and $0.9V_s$ were investigated, where V_{sh} is the shear wave velocity of the saturated ground. The material parameters of the porous medium are the same with Ref [23]. The normalized vertical displacements w^* and pore pressure p^* in the ground at the point (0.0, 1.0, −1.0) under the moving point load were investigated, as shown in Fig. 4. It can be seen from Fig. 4 that the solution by the present approach is in good agreement with those from the literature [23], which illustrates the reliability of the analyze model.

In the following dynamic analysis, the V-G model [45] is used to describe the relationship between the degree of water saturation and the pore suction of the unsaturated soil:

$$S_e = [1 + (\alpha_1 s)^k]^{-m} \tag{34}$$

and the Mualem model [45] is adopted to describe the permeability coefficients of pore water and pore gas:

$$k_w = \frac{\rho_w g \kappa}{\eta_w}\sqrt{S_r}\{1 - [1 - (S_e)^{\frac{1}{m}}]^m\}^2 \tag{35a}$$

$$k_a = \frac{\rho_a g \kappa}{\eta_a}\sqrt{1 - S_r}\left[1 - (S_e)^{\frac{1}{m}}\right]^{2m} \tag{35b}$$

where $\alpha_1 = 1 \times 10^{-5}$, $k = 4$, $m = 1\text{-}1/k = 0.75$ are fitting parameters in the Mualem model; $S_e = (S_r\text{-}S_{w0})/(1\text{-}S_{w0})$ is the effective saturation, where $S_{w0} = 0.05$ is the irreducible saturation of water; $\eta_w = 1.0 \times 10^{-3}$Pa·s, $\eta_a = 1.5 \times 10^{-5}$Pa·s are the viscosity coefficients of pore water and pore gas; $K_w = 2.1 \times 10^9$ N/m^2, $K_a = 1 \times 10^5$ N/m^2 are the bulk modulus of pore water and pore gas; $\kappa = 1.0\,\mu$m^2 is the intrinsic

Table 1
Parameters of foundation soil [13].

Soil layers	Thickness/(m)	Density/(kg/m^3)	Shear wave velocity/(m/s)	Poission's ratio
Crust	1.0	1500	72	0.39
Organic clay	3.0	1260	41	0.35
Clay layer 1	4.5	1475	65	0.41
Clay layer 2	15.0	1475	87	0.33

Table 2
Train axle load distribution of X2000 [13].

Carriage No.	P_{n1}/(kN)	P_{n2}/(kN)	a_n/(m)	b_n/(m)	L_i/(m)
1	160.5	117.5	2.9	11.6	0.0
2	122.5	122.5	2.9	14.8	22.2
3	122.5	122.5	2.9	14.8	24.4
4	122.5	122.5	2.9	14.8	24.4
5	180.0	181.5	2.9	6.6	24.4

Table 3
Track parameters of X2000 [14].

Properties	Values
Track width 2B/m	3
Mass density M/t·m^{-1}	10.8
Bending rigidity EI/MN·m^2	200
Damping ratio	0.10

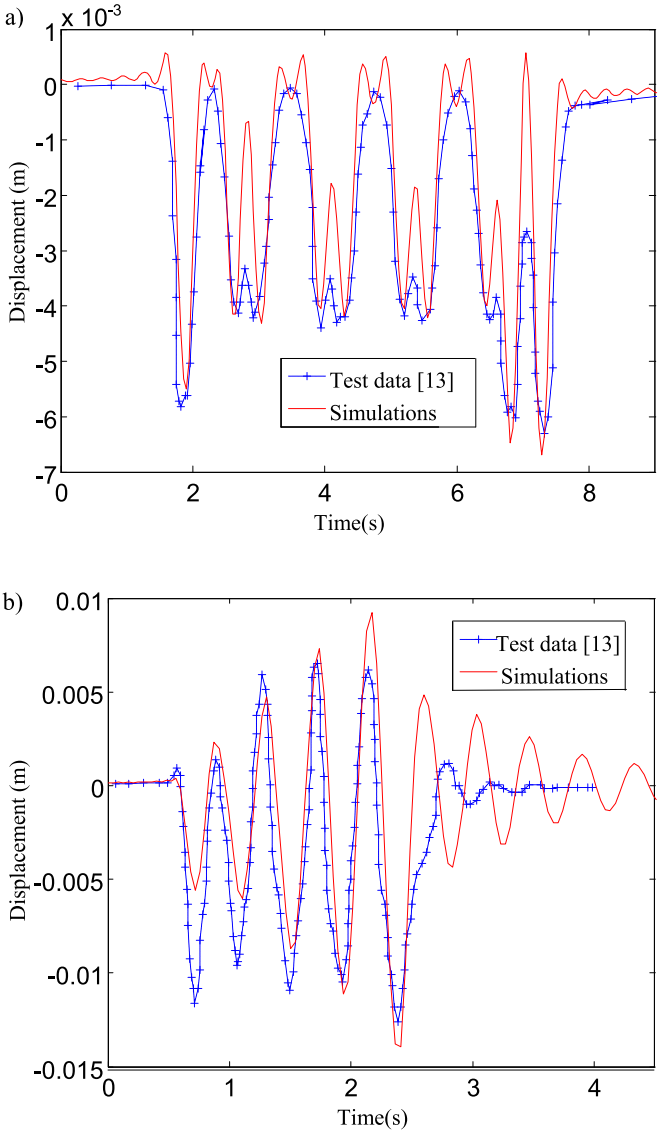

Fig. 3. Time history of ground vertical displacement at the track center for both test data and simulations with different train speeds: a) 70 km/h, b) 200 km/h.

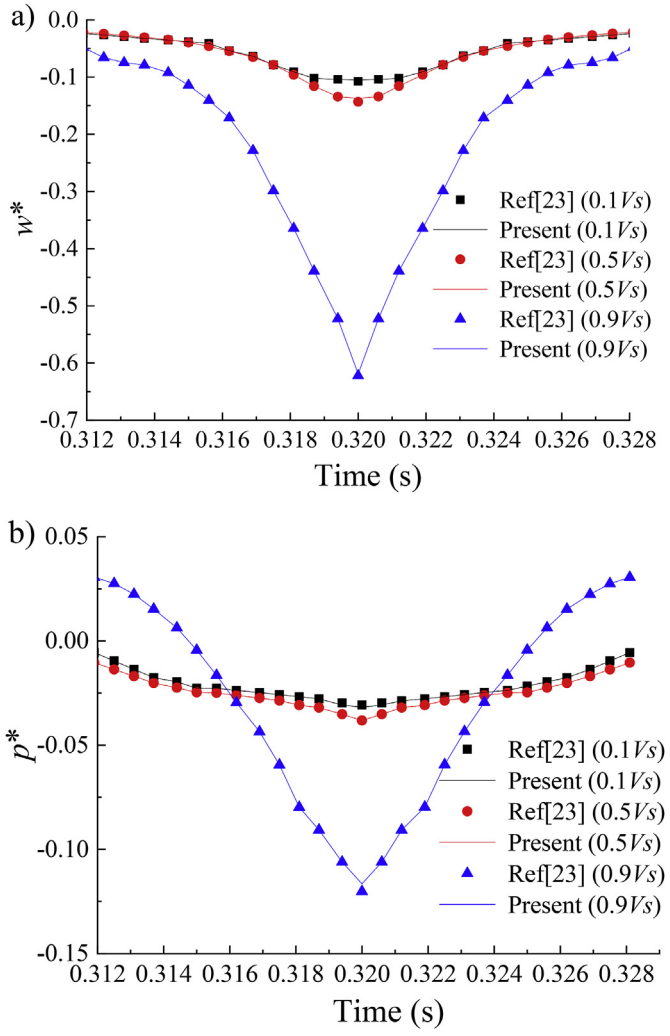

Fig. 4. Verification of 2.5D FEM for saturated soil: a) Displacement time curve; b) Pore pressure time curve.

permeability of soil. The ground surface is set as the drainage and exhaust boundaries, while the bottom and infinite side of the subgrade are set up as non-drainage and non-exhaust boundaries. In this present paper, the high saturation condition (S_r = 100%, 99% and 90%) for the ground is investigated, and more results of the other wide range saturation conditions will be reported in a subsequent paper.

4. Ground vibration at different train speeds

Fig. 5 is the time history of vertical displacement of ground surface at the track center with different degrees of water saturation and train speeds. When the speed is 200 km/h and 250 km/h (Fig. 5-a, -b), the saturated ground displacement is substantially larger than that of unsaturated. The displacement amplitude decreases largely when the degree of water saturation changes from 100% (fully saturated) to 99% (nearly saturated), although the reduction of the degree of water saturation is quite small (1%). The completely phase change of the soil (from three phase of nearly saturated to two phase of fully saturated) brings a completely change of the dynamic characteristics of the soil. However, the displacement amplitude has almost no change when the degree of water saturation reduces from 99% to 90%. From Fig. 5 it can be also seen that, for a given speed (Fig. 5-a, -b, -c, -d), the vibration displacement of unsaturated ground attenuates faster with time than the saturated ground. The pore gas in the soil increased the dissipation rate of the vibration energy. As the train speed increases, the vibration duration time of unsaturated ground becomes shorter, while that of saturated ground changes slightly.

Fig. 6 is the vertical displacement amplitude of ground surface vibration at the track center with different degrees of water saturation and train speeds. It can be seen that both train speed and the pore gas influence the displacement of the soil. As the train speed increases, the saturated ground displacement decreases and then keeps almost constant, while for unsaturated ground the influence of the train speed is not so obvious. When the train speed is larger than 275 km/h, the displacement of unsaturated soil is slightly larger than that of the saturated soil, which is consistent with the conclusion obtained by Theodorakopoulos [21]. The reason may be that at higher train speeds the saturated pore water damping effect is stronger, and that the gas entrance allows the solid to undertake a greater portion of the applied load [21]. When the speed is less than 275 km/h, the displacement of unsaturated soil is substantially lower than that of the saturated soil (as mentioned in Fig. 5), which shows a contrary phenomenon with Ref [21]. This may be caused by the difference between Biot theory used in Ref. [21] and the present three-phase theory, in which the movement of the pore water and pore gas satisfy Darcy's law respectively, and the displacement of soil skeleton at low speed is speculated to be hindered by the movement of pore gas and pore water and their combined damping. For controlling the ground vibration displacement amplitude at the track center in the region with high degree of saturation (S_r = 90%–100%), the train speed is recommended to maintain at about 300–350 km/h. It can also be seen that, for the unsaturated ground, the influence of degree of water saturation on the displacement amplitude is not that obvious when S_r = 90%–99%.

Fig. 7 is the time history of vertical acceleration of ground surface at the track center with different degrees of water saturation and train speeds. It can be seen that at a given speed, the unsaturated ground acceleration is much larger than that of the saturated one, and the unsaturated ground acceleration at S_r = 90% has little difference with that at S_r = 99%. When the train speeds increase from 200 km/h to 250 km/h, both saturated and unsaturated ground accelerations amplitude are greatly reduced by approximately 43% and 52%, respectively. When the train speed increases from 250 km/h to 350 km/h, the unsaturated and saturated ground accelerations amplitude almost has no change. At a given train speed, the unsaturated ground acceleration attenuated faster with time compared to the saturated one; as the train speed increases, the unsaturated ground vibration duration time gradually becomes shorter, while that of saturated ground changes slightly.

Fig. 8 is the time history of vertical acceleration of ground surface at 8 m away from track center (shown as point A in Fig. 2) with different degrees of water saturation and train speeds. The unsaturated ground acceleration at S_r = 90% and 99% is almost the same at the same speed, and both are larger than that of the saturated one. With the increasing of train speed, the unsaturated ground acceleration amplitude gradually becomes smaller. It can also be seen from Fig. 8 (-a, -b) that, when the train speed is 200 km/h or 250 km/h, it takes shorter time for the saturated ground acceleration attenuates to zero than the unsaturated one; while at 300 km/h or 350 km/h Fig. 8 (-c, -d), it takes longer time for the saturated ground acceleration attenuates to zero. As the train speed increases, the unsaturated ground vibration duration time becomes shorter, whereas for saturated ground the duration time gradually becomes longer. It can be observed from Figs. 7 and 8 that, the ground acceleration of the unsaturated soil is larger than that of the saturated soil at both the track center and 8 m away from the track center. This may be caused that, as pointed by Theodorakopoulos [21], a small amount of gas entrance into the saturated ground will greatly reduce the soil stiffness.

Fig. 9 is the acceleration spectrum at 8 m away from the track center with different degrees of water saturation and train speeds. Low frequency vibration (ranged 2–13 Hz) is observed in both unsaturated and saturated ground. For the saturated ground, the vibration components at 2 Hz enhanced as the train speeds increase. While for the unsaturated

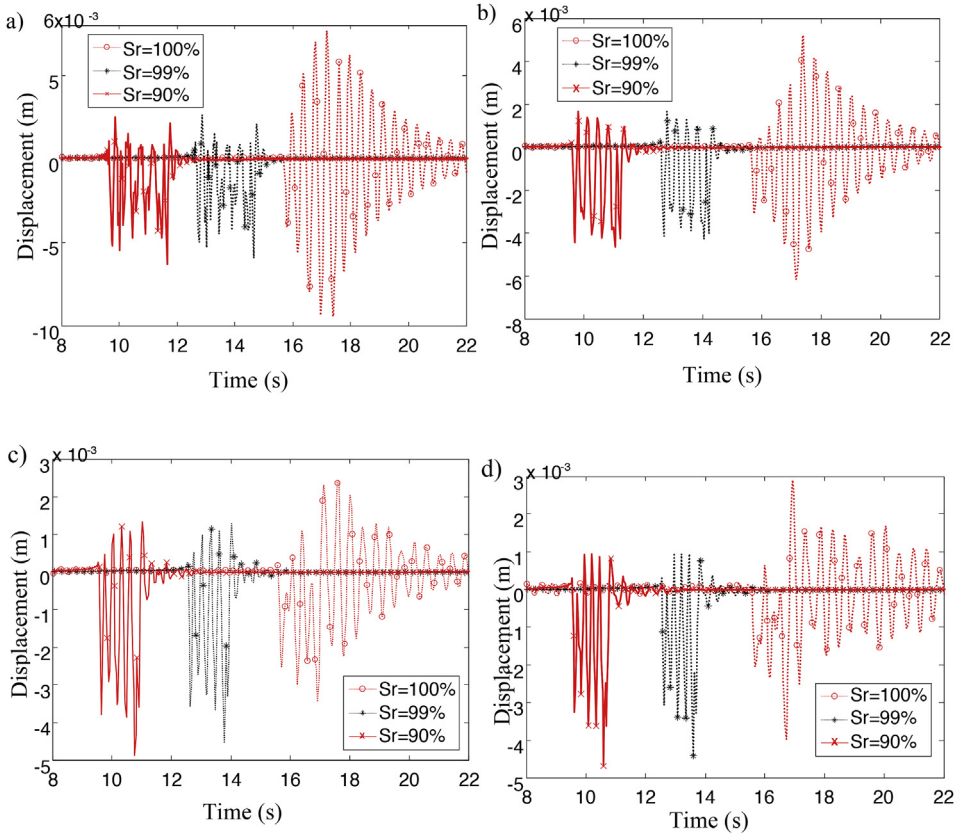

Fig. 5. Time history of vertical displacement of ground surface at the track center with different degrees of water saturation and train speeds: a) 200 km/h, b) 250 km/h, c) 300 km/h, d) 350 km/h.

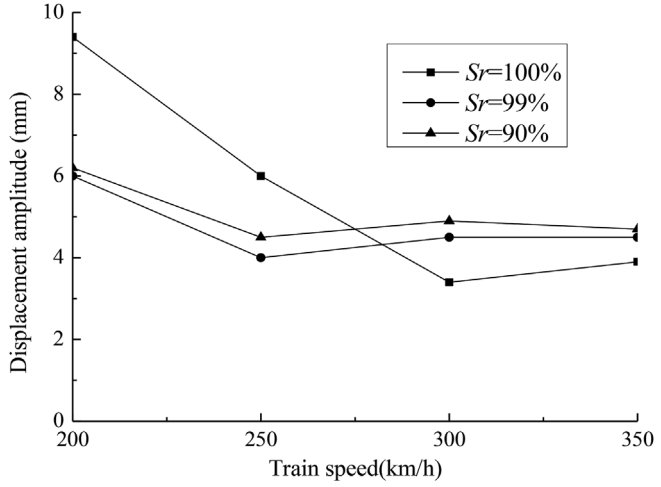

Fig. 6. Vertical displacement amplitude of ground surface at the track center with different degrees of water saturation and train speeds.

ground, the acceleration spectrum varies complicatedly. When the speeds are 200 km/h and 250 km/h, the dominant frequency of unsaturated ground is between 6.6 and 8.6 Hz, and the corresponding accelerations are much larger than that of the saturated one. As the train speeds increase to 300 km/h and 350 km/h, the dominant frequency of both saturated and unsaturated ground decrease significantly to 3.0–3.8 Hz; and the corresponding acceleration of saturated ground tend to be as large as the unsaturated ground.

Fig. 10 is the ground vertical displacement amplitude at 8 m away from the track center with different degrees of water saturation and train speeds. It can be seen that: the saturated ground displacement increases with the train speed increasing; while the unsaturated ground displacement reaches the maximum value at the train speed of 250 km/h and then decreases. The unsaturated ground displacement is larger than that of saturated one at low speed, which is consistent with the conclusion obtained by Ref. [21], and tends to be as large as the saturated one when the speed exceeds 330 km/h. This indicates that, dynamic displacement of the unsaturated ground is complicatedly influenced by many factors, including train speed, the pore gas, and distance from the moving load, etc.

5. Attenuation of ground vibration at different train speeds

Fig. 11 shows the attenuation of the ground vertical displacement amplitude with distance from the track center at different train speeds at S_r = 90%. Within 5 m from the track center (near the track), the ground displacement amplitude at 200 km/h is greater than that in the other speeds. Near the track, the ground displacements attenuate rapidly with almost the same rate at both high and low train speeds. Beyond 5 m from the track center, the displacement amplitude at each high speed is almost equal and non-attenuated except at 200 km/h. The ground vertical displacement attenuates very slowly beyond a certain distance (about 6 m away from the track center) at high train speed.

6. Excess pore water pressures at different train speeds

Fig. 12 is the time history of excess pore water pressure at 0.5 m depth beneath the track center. Before the train pass, the pore water pressure at S_r = 99% is negative, and at S_r = 90% it is zero. At the same train speed, the excess pore water pressure amplitude increases sharply with the degree of water saturation increasing, and it is about 5 times at S_r = 99% than that at S_r = 90%. The train loads may cause larger excess pore water pressure in the nearly saturated ground (S_r = 99%).

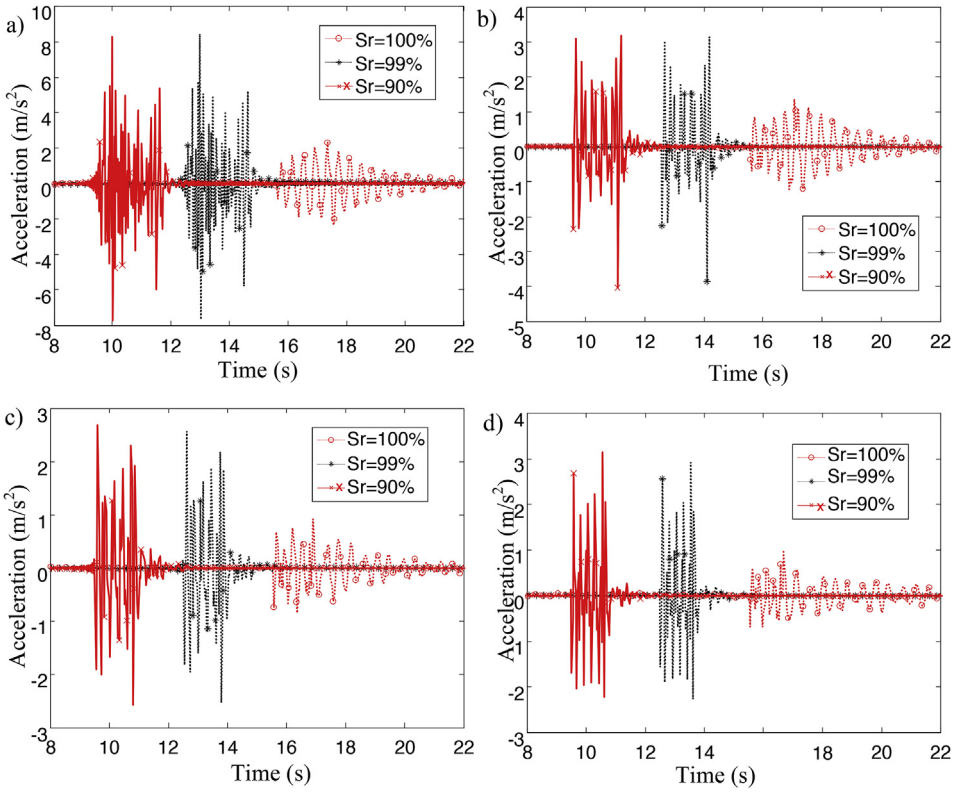

Fig. 7. Time history of vertical acceleration of ground surface at the track center with different degrees of water saturation and train speeds: a) 200 km/h, b) 250 km/h, c) 300 km/h, d) 350 km/h.

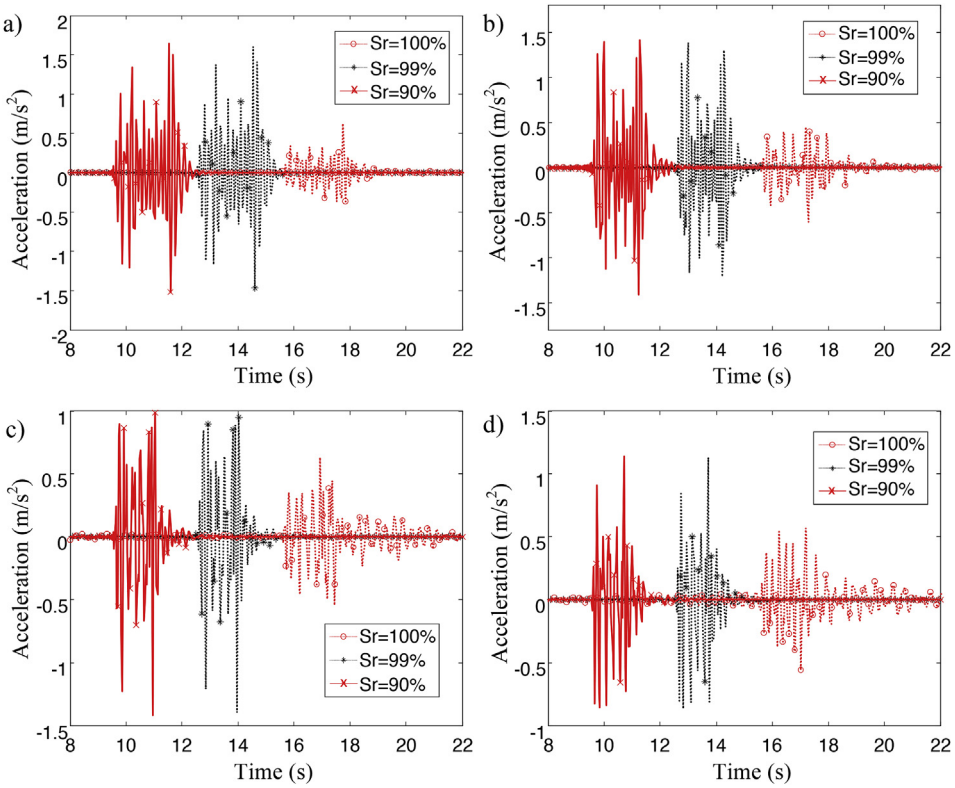

Fig. 8. Time history of vertical acceleration of ground surface at 8 m away from the track center with different degrees of water saturation and train speeds: a) 200 km/h, b) 250 km/h, c) 300 km/h, d) 350 km/h.

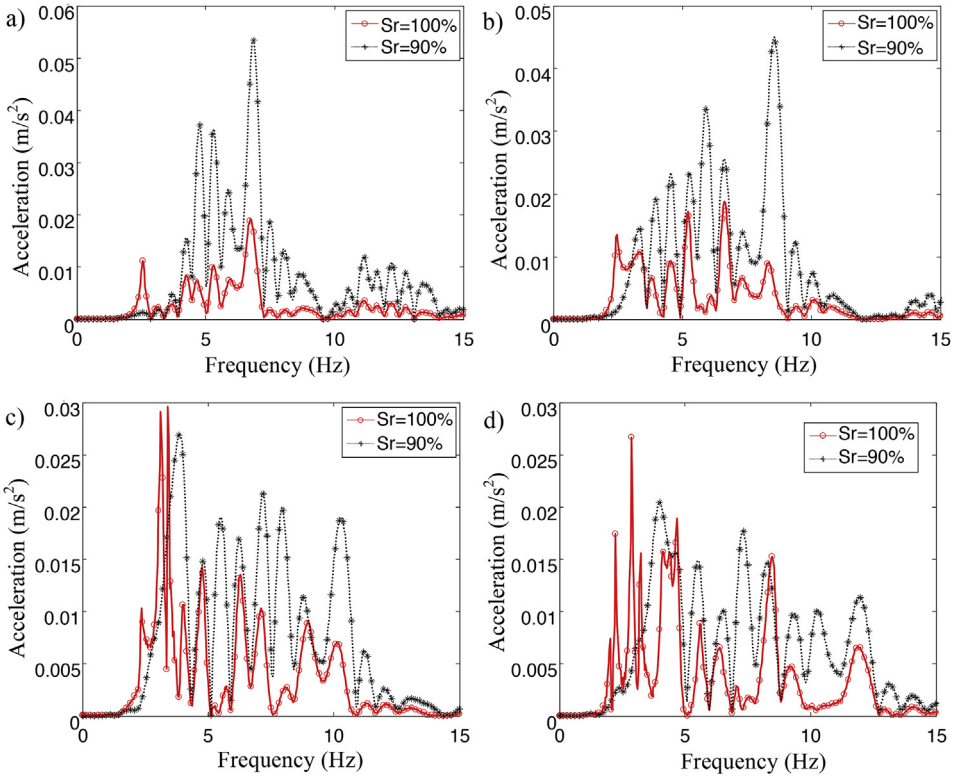

Fig. 9. Ground acceleration spectrum at 8 m away from the track center with different degrees of water saturation and train speeds: a) 200 km/h, b) 250 km/h, c) 300 km/h, d) 350 km/h.

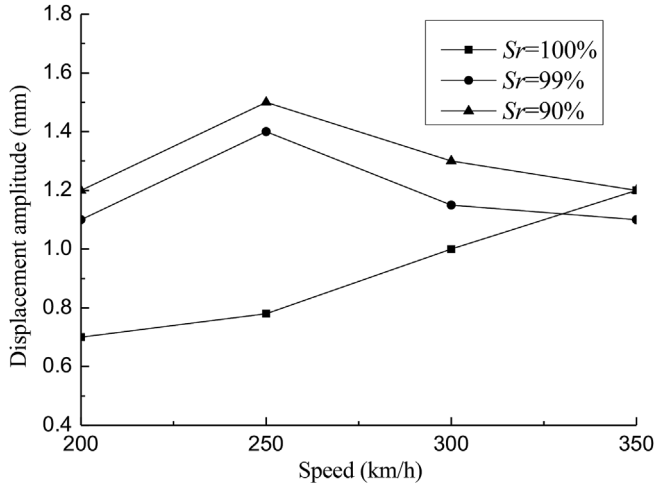

Fig. 10. Ground vertical displacement amplitude at 8 m away from the track center with different degrees of water saturation and train speeds.

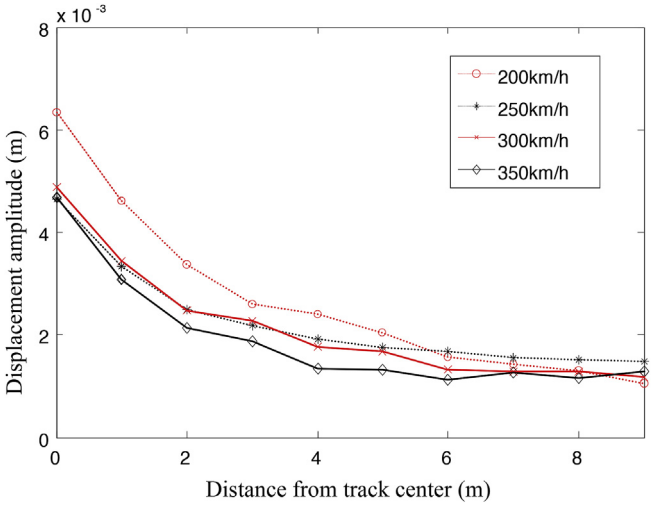

Fig. 11. Attenuation of the ground displacement amplitude with distance from the track center at different train speeds (Sr = 90%).

Moreover the excess pore water pressure decreases little as the train speed increases.

Fig. 13 is the excess pore water pressure distributed with depth beneath the track center at different train speeds. It can be found that the excess pore water pressure of unsaturated ground decreases sharply at about 3.5–4.0 m. The development of excess pore water pressure of unsaturated ground at S_r = 90% prevails in the shallow depth (within 4.0 m), and at S_r = 99% it mainly distributes within 8 m, which is much deeper than that at S_r = 90%. At the same speed, the amplitude of excess pore water pressure at S_r = 99% is much larger than its counterparts at S_r = 90%, and the maximum amplitude of excess pore water pressure is located at 1.5–2.0 m depth and decreases significantly as the degree of water saturation decreases.

Fig. 14 shows the excess pore water pressure amplitude varies with train speeds beneath the track center. We can see that, at the same speed, the amplitude of excess pore water pressure at Sr = 99% is much larger than that at Sr = 90%. With the train speed increases from 200 km/h to 350 km/h, the excess pore water pressure at Sr = 99% decreases slightly and then keeps almost constant; while at Sr = 90%, the excess pore water pressure varies little with the train speed increasing. Therefore, the train speed is recommended to maintain between 250 and 350 km/h to reduce the excess pore water pressure amplitude beneath the track center in coastal area of China, where soil with high degree of water saturation is widely distributed.

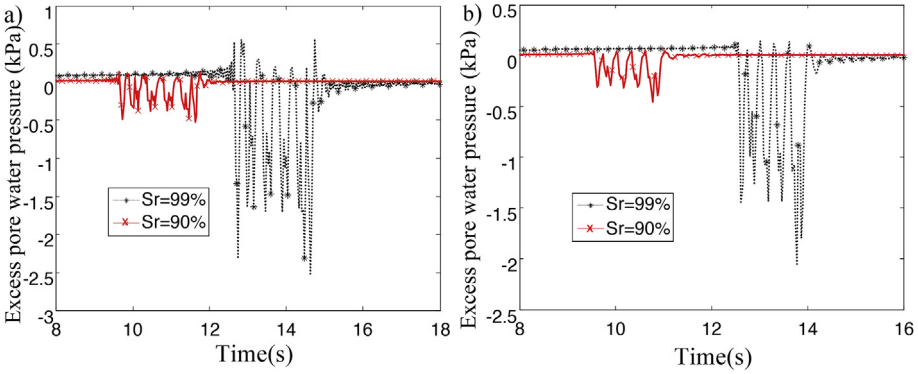

Fig. 12. Time history of the excess pore water pressure at 0.5 m depth beneath the track center at different train speeds: a) 200 km/h, b) 300 km/h.

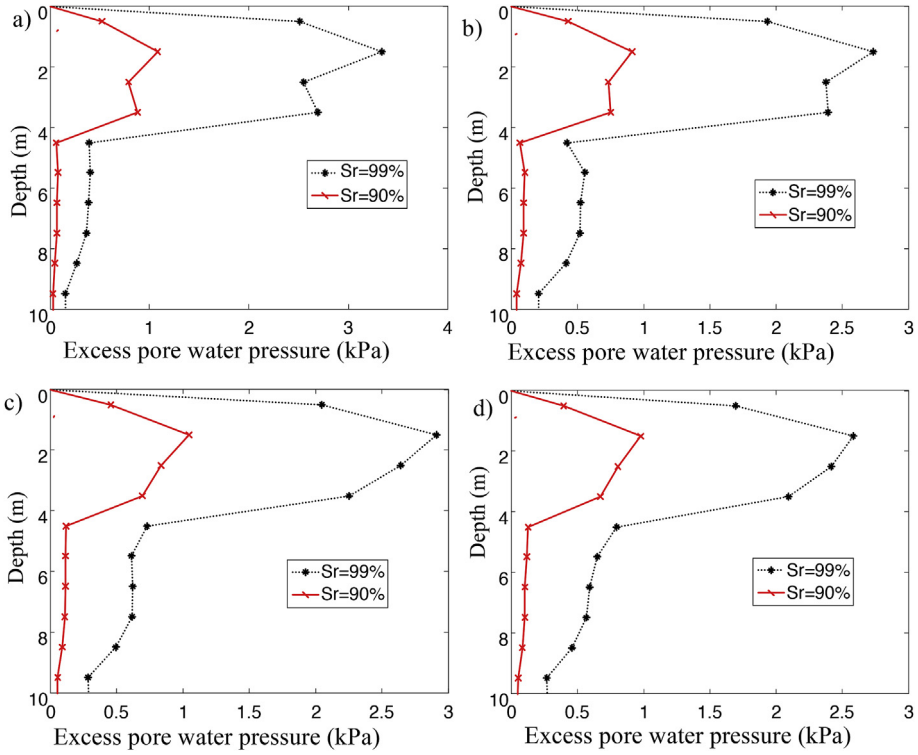

Fig. 13. Distribution of excess pore water pressure with depth beneath the track center at different train speeds: a) 200 km/h, b) 250 km/h, c) 300 km/h, d) 350 km/h.

7. Conclusions

This paper presents an efficient 2.5D FEM formulation for analyzing the three-phase unsaturated ground vibration induced by high-speed trains. Effects of the degree of water saturation and the train speed have been investigated and the following conclusions can be drawn:

(1) At the track center, a very small amount of gas in the saturated ground largely increases the ground acceleration amplitude. The gas phase has varied influence to the ground displacement amplitude at different train speed level. The saturated ground displacement is larger than the unsaturated one when the speed is less than 275 km/h. Dynamic displacement of the unsaturated ground is complicatedly influenced by many factors, including train speed, the pore gas, and distance from the moving load, etc. The vibration displacement of unsaturated ground attenuates faster with time than the saturated ground. The unsaturated ground vibration at S_r = 90% has little difference with that at S_r = 99% at the same train speed.

(2) At 8 m away from the track center, the acceleration amplitude of unsaturated ground is larger than the saturated one. The ground acceleration of unsaturated ground attenuates faster than the saturated one as the train speed is larger than 330 km/h. As the train speed increases, the dominant frequency of both saturated and unsaturated ground decreases.

(3) At 8 m away from the track center, the unsaturated ground displacement is larger than that of saturated one at low train speeds. The saturated ground displacement increases as the train speed increases, whereas for unsaturated ground it increases and then decreases.

(4) Within 5 m from the track center, the ground displacement amplitude at low train speed is larger than the high train speeds; ground displacements attenuate rapidly with almost the same rate for both high and low train speeds.

(5) The excess pore water pressure of unsaturated ground beneath the track center distributes deeper as the degree of water saturation increases. The maximum excess pore water pressure amplitude is located at 1.5–2.0 m depth and decreases significantly as the degree

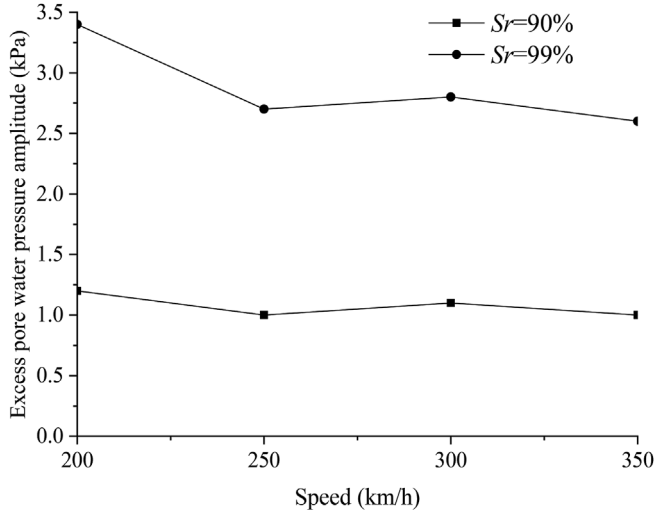

Fig. 14. Variation of excess pore water pressure amplitude with train speeds beneath the track center.

of water saturation decreases. The train speed is recommended to maintain between 250 and 350 km/h on the ground with high degree of water saturation, in order to reduce the excess pore water pressure amplitude beneath the track center.

Acknowledgements

The project was supported by the National Natural Science Foundation of China (No. 41772288), which is gratefully acknowledged.

Appendix C. Supplementary data

Supplementary data to this article can be found online at https://doi.org/10.1016/j.soildyn.2019.05.034.

Notation

a_n, b_n	distances between axles
B	B(—)partial derivative matrices to skeleton displacement and pore pressure of unsaturated soil
B	*, B(—)* conjugate matrix of the **B** and B(—)
D	elastic matrix
EI	bending stiffness of the track system
$\tilde{f}_{TT}(\xi_x, \omega)$	contact reaction force of the ground
$\tilde{\mathbf{f}}_{\mathbf{up}}$, $\tilde{\mathbf{f}}_{\mathbf{up}}$	pore water and gas flux matrix in frequency-wave number domain
$\tilde{\mathbf{f}}^{\mathbf{s}}_{\mathbf{up}}$	equivalent nodal force matrix in frequency-wave number domain
F_w, F_a	parameters in Eq. (15) and Eq. (16)
g	gravity acceleration
G′	**G**pore gas contribution matrices
J	Jacobi matrix
|J|	determinant of **J**
k_w, k_a	permeability coefficient of the pore water and pore gas
K_{sk}, K_g	bulk modulus of soil skeleton and soil particle, respectively
K_w, K_a	bulk modulus of the pore water and pore gas, respectively
K	the total assembled stiffness matrix
K	‘$_{\mathbf{up}}$, $\mathbf{M}_{\mathbf{up}}$ stiffness matrix and mass matrices
L_0	distance to a reference position ahead of the first axle load position
L_i	length of the *i*th car (i = 1, 2, 3, 4, 5)
m	comprehensive quality of the track and sleepers
n	porosity of the unsaturated soil
n_j	exterior normal direction vector of the boundary
N	car numbers of the moving train
N_i	shape function
N	$\bar{\mathbf{N}}$ shape function matrix of skeleton displacement and pore pressure of unsaturated soil
p_c	equivalent pore pressure of the unsaturated soil
p^w, p^a	pressure of the pore water and pore gas, respectively
$\tilde{p}_0(\xi_x, \omega)$	dynamic train load on the track in frequency-wave number domain
P_{n1}, P_{n2}	axle loads for the front and rear bogies
Q′	**Q** pore water contribution matrices
R	the total assembled equivalent nodal force matrix
s	p^a-p^w is matric suction of unsaturated soil
S_r	the degree of water saturation
S_e	effective degree of water saturation of the unsaturated ground
S_{w0}	irreducible degree of water saturation

S_σ stress boundary
S_p flux boundary
t time variable
T_i, p^f stress and pore pressure at the boundary, where $f = w, a$ represent pore water and pore gas, respectively
u^e, p^{we}, p^{ae} nodal displacement, nodal pore water pressure and gas pressure
u_i, u^w, u^a displacement of the soil particle, pore water and pore gas
$\tilde{u}_r$ track displacement in frequency-wave number domain
$\mathbf{U}$ the total assembled unknown variable matrix
$\mathbf{v}_f$ fluid velocity at the boundary S_p;
V_c train moving velocity
V_s shear-wave velocity of the saturated ground
w^*, p^* normalized vertical displacements in the ground at the point (0.0, 1.0, −1.0) under the moving point load
x space variable of train moving direction
α Biot coefficient
α_1, k, m fitting parameters of V-G model
δ_{ij} Kronecker symbol
η, ξ local coordinates
η_i, ξ_i node coefficients in local coordinates
η_s damping coefficient of the unsaturated soil
η_w, η_a viscosity coefficients of pore water and pore gas
κ intrinsic permeability of soil
λ, μ Lame constants of the unsaturated soil
λ^c, μ^c complex form of the Lame constants
ρ_s, ρ_w, ρ_a density of the soil particle, pore water and pore gas
σ_{ij}, ε_{ij} total stress tensor, strain tensor of the unsaturated soil
$\chi(\xi_x)$ parameters in Eq. (33)
ω frequency variable corresponding to t
ξ_x wave number variable corresponding to x
$\delta\tilde{u}_i^*$ $\delta\tilde{p}_i^f$ variation of the virtual displacement and virtual pore pressure
"~" variables in frequency domain
"-" variables in wave number domain
"." first order derivative with time;
".." second order derivative with time;
"T" transpose of the matrix

Appendix A. The detailed coefficients in Eqs. (8) and (12)

$$A_{11} = \frac{(\alpha - n)S_r^2}{K_g} + \frac{nS_r}{K_w} - A_{ss}\left(n - \frac{s(\alpha - n)S_r}{K_g}\right);\ A_{12} = \frac{(\alpha - n)S_r(1 - S_r)}{K_g} + A_{ss}\left(n - \frac{s(\alpha - n)S_r}{K_g}\right)$$

$$A_{13} = S_r(\alpha - n);\ A_{14} = nS_r;\ A_{ss} = \frac{\partial S_r}{\partial s}$$

$$A_{21} = \frac{(\alpha - n)S_r(1 - S_r)}{K_g} + A_{ss}\left(n + \frac{(\alpha - n)(1 - S_r)s}{K_g}\right)$$

$$A_{22} = \frac{(\alpha - n)(1 - S_r)^2}{K_g} + \frac{n(1 - S_r)}{K_a} - A_{ss}\left(n + \frac{(\alpha - n)(1 - S_r)s}{K_g}\right)$$

$$A_{23} = (1 - S_r)(\alpha - n);\ A_{24} = n(1 - S_r)$$

$$A_{31} = \omega^2\left[(1 - n)\rho_s + nS_r\rho_w\frac{F_w}{F_w - \rho_w\omega^2} + n(1 - S_r)\rho_w\frac{F_a}{F_a - \rho_a\omega^2}\right]$$

$$A_{32} = \frac{\omega^2 nS_r\rho_w}{F_w - \rho_w\omega^2};\ A_{33} = \frac{\omega^2 n(1 - S_r)\rho_a}{F_a - \rho_a\omega^2}$$

Appendix B. The detailed elements of K and R in Eq. (31):

$$\mathbf{K} = \begin{bmatrix} \mathbf{K'_{up}} - \mathbf{M_{up}} & \mathbf{Q'_{up}} - \mathbf{Q_{up}} & \mathbf{G'_{up}} - \mathbf{G_{up}} \\ \mathbf{H_{md}} & \mathbf{Q_{md}} + \mathbf{Q'_{md}} & \mathbf{G'_{md}} \\ \mathbf{H_{dw}} & \mathbf{Q'_{dw}} & \mathbf{G'_{dw}} + \mathbf{G_{dw}} \end{bmatrix} \mathbf{R} = \begin{bmatrix} \tilde{\mathbf{f}}^{\mathbf{s}}_{\mathbf{up}} \\ \tilde{\mathbf{f}}^{\mathbf{w}}_{\mathbf{up}} \\ \tilde{\mathbf{f}}^{\mathbf{a}}_{\mathbf{up}} \end{bmatrix}$$

$$K'_{up} = \sum_e \iint (B^*N)^T D(BN)|J|d\eta d\xi$$

$$\mathbf{M_{up}} = A_{31} \sum_e \iint \mathbf{N}\mathbf{N}^T|\mathbf{J}|d\eta d\xi$$

$$Q_{up} = \alpha S_r \sum_e \iint (B^*N)^T m\bar{N}|J|d\eta d\xi$$

$$Q_{up} = \alpha S_r \sum_e \iint (B^*N)^T m\bar{N}|J|d\eta d\xi$$

$$\mathbf{G'_{up}} = A_{33} \sum_e \iint \mathbf{N}^T\bar{\mathbf{B}}\bar{\mathbf{N}}|\mathbf{J}|d\eta d\xi$$

$$\mathbf{G_{up}} = \alpha(1 - S_r) \sum_e \iint (\mathbf{B^*N}\Big)^T \mathbf{m}\bar{\mathbf{N}}|\mathbf{J}|d\eta d\xi$$

$$\mathbf{H_{md}} = \left(A_{13} + \frac{A_{14}F_w}{F_w - \rho_w\omega^2}\right) \sum_e \iint \bar{\mathbf{N}}^{\mathbf{T}}\bar{\mathbf{B}}^{\mathbf{T}}\mathbf{N}|\mathbf{J}|d\eta d\xi$$

$$Q_{md} = \frac{A_{14}}{F_w - \rho_w\omega^2} \sum_e \iint (\bar{B}^*\bar{N})^T(\bar{B}\bar{N})|J|d\eta d\xi$$

$$\mathbf{Q'_{md}} = A_{11} \sum_e \iint \bar{\mathbf{N}}^{\mathbf{T}}\bar{\mathbf{N}}|\mathbf{J}|d\eta d\xi$$

$$\mathbf{G'_{md}} = A_{12} \sum_e \iint \bar{\mathbf{N}}^{\mathbf{T}}\bar{\mathbf{N}}|\mathbf{J}|d\eta d\xi$$

$$\mathbf{H_{dw}} = \left(A_{23} + \frac{A_{24}F_a}{F_a - \rho_a\omega^2}\right) \sum_e \iint \bar{\mathbf{N}}^{\mathbf{T}}\bar{\mathbf{B}}^{\mathbf{T}}\mathbf{N}|\mathbf{J}|d\eta d\xi$$

$$\mathbf{Q'_{dw}} = A_{21} \sum_e \iint \bar{\mathbf{N}}^{\mathbf{T}}\bar{\mathbf{N}}|\mathbf{J}|d\eta d\xi$$

$$\mathbf{G'_{dw}} = A_{22} \sum_e \iint \bar{\mathbf{N}}^{\mathbf{T}}\bar{\mathbf{N}}|\mathbf{J}|d\eta d\xi$$

$$G_{dw} = \frac{A_{24}}{F_a - \rho_a\omega^2} \sum_e \iint (\bar{B}^*\bar{N})^T(\bar{B}\bar{N})|J|d\eta d\xi$$

$$\tilde{\mathbf{f}}^{\mathbf{s}}_{\mathbf{up}} = \sum_e \iint \mathbf{N}^T\tilde{\mathbf{T}}|\mathbf{J}|d\eta d\xi$$

$$\tilde{\mathbf{f}}^{\mathbf{w}}_{\mathbf{up}} = -\frac{A_{14}}{F_w - \rho_w\omega^2} \sum_e \iint \bar{\mathbf{N}}^{\mathbf{T}}\frac{\rho_w g\tilde{\mathbf{v}}_{\mathbf{w}}}{k_w}|\mathbf{J}|d\eta d\xi$$

$$\tilde{\mathbf{f}}^{\mathbf{a}}_{\mathbf{up}} = -\frac{A_{24}}{F_a - \rho_a\omega^2} \sum_e \iint \bar{\mathbf{N}}^{\mathbf{T}}\frac{\rho_a g\tilde{\mathbf{v}}_{\mathbf{a}}}{k_a}|\mathbf{J}|d\eta d\xi$$

$$\mathbf{D} = \begin{bmatrix} \lambda^c + 2\mu^c & \lambda^c & \lambda^c & 0 \\ & \lambda^c + 2\mu^c & \lambda^c & 0 \\ & & \lambda^c + 2\mu^c & 0 \\ & & & \mathbf{I}_3\mu^c \end{bmatrix};\ \mathbf{B} = \begin{bmatrix} -i\xi_x & 0 & 0 & \frac{\partial}{\partial y} & 0 & \frac{\partial}{\partial z} \\ 0 & \frac{\partial}{\partial y} & 0 & -i\xi_x & \frac{\partial}{\partial z} & 0 \\ 0 & 0 & \frac{\partial}{\partial z} & 0 & \frac{\partial}{\partial y} & -i\xi_x \end{bmatrix}^T;\ \bar{\mathbf{B}} = \begin{pmatrix} -i\xi_x \\ \frac{\partial}{\partial y} \\ \frac{\partial}{\partial z} \end{pmatrix}$$

References

[1] Beskou ND, Theodorakopoulos DD. Dynamic effects of moving loads on road pavements: a review. Soil Dynam Earthq Eng 2011;31(4):547–67.
[2] Eason G. The stresses produced in a semi-infinite solid by a moving surface force. Int J Eng Sciences 1965;2(6):581–609.
[3] Lu Z, Hu Z, Yao HL, Liu J, Zhan YX. An analytical method for evaluating highway embankment responses with consideration of dynamic wheel–pavement interactions. Soil Dynam Earthq Eng 2016;83:135–47.
[4] Sheng X, Jones CJC, Petyt M. Ground vibration generated by a load moving along a railway track. J Sound Vib 1999;228(1):129–56.
[5] Ekevid T, Li MXD, Wiberg NE. Adaptive FEA of wave propagation induced by high-speed trains. Comput Struct 2001;79:2693–704.
[6] Rasmussen KM, Nielsen SRK, Kirkegaard PH. Boundary element method solution in the time domain for a moving time-dependent force. Comput Struct 2001;79:691–701.
[7] Andersen L, Nielsen SRK. Boundary element analysis of steady-state response of elastic half-space to a moving force on its surface. Eng Anal Bound Elem 2003;27:23–38.
[8] Pan G, Atluri SN. Dynamic response of finite sized elastic runways subjected to moving loads: a coupled BEM/FEM approach. Int J Numer Methods Eng 1995;38:3143–66.
[9] Yang YB, Hung HH. A 2.5D finite/infinite element approach for modeling visco-elastic bodies subjected to moving loads. Int J Numer Methods Eng 2001;51(11):1317–36.
[10] Yang YB, Hung HH, Chang DW. Train-induced wave propagation in multi- layered soils using finite/infinite element simulation. Soil Dynam Earthq Eng 2003;23(4):263–78.
[11] Hwang RN, Lysmer J. Response of buried structures to traveling waves. J Geotech

Eng Div 1981;107(2):183–200.
[12] Barros FCPD, Luco JE. Response of a layered viscoelastic half-space to a moving point load. Wave Motion 1994;19(2):189–210.
[13] Takemiya H. Simulation of track–ground vibrations due to a high-speed train: the case of X-2000 at ledsgard. J Sound Vib 2003;261(3):503–26.
[14] Bian XC, Chen YM, Hu T. Numerical simulation of high-speed train induced ground vibrations using 2.5D finite element approach. Sci China Phys Mech Astron 2008;51(6):632–50.
[15] Bian X, Jiang H, Chang C, Hu J, Chen Y. Track and ground vibrations generated by high-speed train running on ballastless railway with excitation of vertical track irregularities. Soil Dynam Earthq Eng 2015;76:29–43.
[16] Biot MA. Theory of propagation of elastic waves in a fluid-saturated porous solid-I: low-frequency range. J Acoust Soc Am 1956;28(2):168–78.
[17] Biot MA. Mechanics of deformation and acoustic propagation in porous media. J Appl Phys 1962;33(4):1482–98.
[18] Jin B, Yue ZQ, Tham LG. Stresses and excess pore pressure induced in saturated poroelastic half space by moving line load. Soil Dynam Earthq Eng 2004;24(1):25–33.
[19] Chen Y, Beskou ND, Qian J. Dynamic response of an elastic plate on a cross- anisotropic poroelastic half-plane to a load moving on its surface. Soil Dynam Earthq Eng 2018;107:292–302.
[20] Siddharthan R, Zafir Z, Norris GM. Moving load response of layered soil. i: formulation & ii: verification and application. J Eng Mech 1993;119(10):2052–89.
[21] Theodorakopoulos DD. Dynamic analysis of a poroelastic half-plane soil medium under moving loads. Soil Dynam Earthq Eng 2003;23(7):521–33.
[22] Theodorakopoulos DD, Chassiakos AP, Beskos DE. Dynamic effects of moving load on a poroelastic soil medium by an approximate method. Int J Solids Struct 2004;41(7):1801–22.
[23] Lu JF, Jeng DS. A half-space saturated poro-elastic medium subjected to a moving point load. Int J Solids Struct 2007;44(2):573–86.
[24] Lefeuve-Mesgouez G, Mesgouez A. Three-dimensional dynamic response of a porous multilayered ground under moving loads of various distributions. Adv Eng Software 2012;46(1):75–84.
[25] Cai YQ, Sun HL, Xu CJ. Response of railway track system on poroelastic half-space soil medium subjected to a moving train load. Int J Solids Struct 2008;45(18–19):5015–34.
[26] Cai YQ, Chen Y, Cao ZG, Sun HL, Guo L. Dynamic responses of a saturated poroelastic half-space generated by a moving truck on the uneven pavement. Soil Dynam Earthq Eng 2015;69:172–81.
[27] Yang SP, Fang XQ, Liu JX. Vibration prediction of water-saturated poroelastic ground induced by high speed train with sleeper effect. Appl Math Model 2015;39(12):3331–40.
[28] Gao GY, Chen QS, He JF, Liu F. Investigation of ground vibration due to trains moving on saturated multi-layered ground by 2.5D finite element method. Soil Dynam Earthq Eng 2012;40(3):87–98.
[29] Gao GY, Song J, Chen GQ, Yang J. Numerical prediction of ground vibrations induced by high-speed trains including wheel-rail-soil coupled effects. Soil Dynam Earthq Eng 2015;77:274–8.
[30] Gao GY, Xu CX, Chen J, Jian S. Investigation of ground vibrations induced by trains moving on saturated transversely isotropic ground. Soil Dynam Earthq Eng 2018;104:40–4.
[31] Fredlund DG, Rahardjo H. Soil mechanics for unsaturated soils. Architecture and Building Press; 1997.
[32] Jafarzadeh F, Sadeghi H. Experimental study on dynamic properties of sand with emphasis on the degree of saturation. Soil Dynam Earthq Eng 2012;32(1):26–41.
[33] Vardoulakis I, Beskos DE. Dynamic behavior of nearly saturated porous media. Mech Mater 1986;5(1):87–108.
[34] Yang J, Sato T. Interpretation of seismic vertical amplification observed at an array site. Bull Seismol Soc Am 2000;90(2):275–85.
[35] Yang J, Sato T. Influence of water saturation on horizontal and vertical motion at a porous soil interface induced by incident SV wave. Soil Dynam Earthq Eng 2000;19(5):339–46.
[36] Yang J. Saturation effects of soils on ground motion at free surface due to incident SV waves. J Eng Mech 2002;128(12):1295–303.
[37] Zhao CB, Valliappan S, Wang YC. A numerical model for wave scattering problems in infinite media due to P and SV wave incidences. Int J Numer Methods Eng 1992;33:1661–82.
[38] Zhao CB, Valliappan S. A dynamic infinite element for three-dimensional infinite-domain wave problems. Int J Numer Methods Eng 1993;36(15):2567–80.
[39] Astley RJ. Infinite elements for wave problems: a review of current formulations and an assessment of accuracy. Int J Numer Methods Eng 2000;49(7):951–76.
[40] Hall WS, Oliveto G. Boundary element methods for soil-structure interaction. Kluwer Academic Publishers; 2003.
[41] Tsynkov SV. Numerical solution of problems on unbounded domains: a review. Elsevier Science Publishers; 1998.
[42] Du XL, Zhao M. A local time-domain transmitting boundary for simulating cylindrical elastic wave propagation in infinite media. Soil Dynam Earthq Eng 2010;30(10):937–46.
[43] Li P, Song EX. A high-order time-domain transmitting boundary for cylindrical wave propagation problems in unbounded saturated poroelastic media. Soil Dynam Earthq Eng 2013;48:48–62.
[44] Wang ZH, Zhao CG, Dong L. An approximate spring-dashpot artificial boundary for transient wave analysis of fluid-saturated porous media. Comput Geotech 2009;36(1–2):199–210.
[45] Genuchten MTV. A closed form equation for predicting the hydraulic conductivity of unsaturated soils. Soil Sci Soc Am J 1980;44(5):892–8.